

Measurement of the infrared complex Faraday angle in semiconductors and insulators

M.-H. Kim, V. Kurz, G. Acbas, C. T. Ellis, and J. Cerne*

Department of Physics, University at Buffalo, The State University of New York, Buffalo, New York 14260, USA

**Corresponding author: jcerne@buffalo.edu*

Received June 15, 2010; accepted July 20, 2010;

posted October 14, 2010 (Doc. ID 130156); published January 5, 2011

We measure the infrared (wavelength $\lambda = 11 - 0.8 \mu\text{m}$; energy $E = 0.1 - 1.5 \text{ eV}$) Faraday rotation and ellipticity in GaAs, BaF₂, LaSrGaO₄, LaSrAlO₄, and ZnSe. Since these materials are commonly used as substrates and windows in infrared magneto-optical measurements, it is important to measure their Faraday signals for background subtraction. These measurements also provide a rigorous test of the accuracy and sensitivity of our unique magneto-polarimetry system. The light sources used in these measurements consist of gas and semiconductor lasers, which cover 0.1 – 1.3 eV, as well as a custom-modified prism monochromator with a Xe lamp, which allows continuous broadband measurements in the 0.28 – 1.5 eV energy range. The sensitivity of this broadband system is approximately 10 μrad . Our measurements reveal that the Verdet coefficients of these materials are proportional to λ^{-2} , which is expected when probing with photon energies below the band gap. Reproducible ellipticity signals are also seen, which is unexpected since the photon energy is well below the absorption edge of these materials, where no magnetic circular dichroism or magnetic linear birefringence should occur. We suggest that the Faraday ellipticity is produced by the static retardance of the photoelastic modulator and other optical elements such as windows, which convert the polarization rotation produced by the sample into ellipticity. This static retardance is experimentally determined by the ratio of the Faraday rotation and ellipticity signals, which are induced by either applying a magnetic field to a sample or mechanically rotating the polarization of light incident on the photoelastic modulator and/or other optical components. © 2011 Optical Society of America

OCIS codes: 120.2130, 120.4530.

1. INTRODUCTION

Faraday measurements probe materials by exploring changes in the polarization of transmitted light. These changes are induced by the presence of a magnetic field or magnetization and are highly sensitive to critical properties such as electronic band structure and spin population. Faraday measurements have been widely performed on semiconductors [1] and, more recently, on III-V diluted magnetic semiconductors [2–5] and high temperature superconductors [6,7] in the visible and infrared energy range. These measurements provide detailed new information which complement conventional infrared conductivity measurements [8]. For example, we have used these techniques to sensitively probe the spin-dependent electronic structure of Ga_{1-x}Mn_x as near the Fermi energy [9]. The Faraday effect in many optical materials such as GaAs, BaF₂, LaSrGaO₄, LaSrAlO₄, and ZnSe, is well studied in the visible and near-infrared range. However, similar mid-infrared (MIR, wavelength $\lambda = 11 - 2 \mu\text{m}$; energy $E = 0.1 - 0.6 \text{ eV}$) Faraday measurements have been rare. Understanding the nature of these materials in the MIR is extremely important because they are commonly used as substrates, windows, and lenses in studies of more remarkable materials such as high-temperature superconducting cuprates (HTSC) [6,7] and III-V(Mn) diluted magnetic semiconductors, [9–12], which are particularly revealing in this spectral regime. The key features of the measurements presented in this paper are what is to our knowledge the first report of the MIR Verdet constant for BaF₂ and LaSrAlO₄; measurement of both Faraday rotation and ellipticity; and a broad nearly continuous infrared spectral range. Furthermore, since we are developing new instrumen-

tation and techniques, these measurements provide an excellent test of the accuracy and sensitivity of our magneto-polarimetry system.

Magneto-optical transmission measurements with the magnetic field and radiation propagation directions both oriented perpendicular to the sample surface, determine the complex Faraday angle produced by a sample in a magnetic field. The real part of the Faraday angle $\text{Re}(\theta_F)$ is related to the rotation of the plane of polarization (Faraday rotation) and the imaginary part $\text{Im}(\theta_F)$ is connected to the ellipticity (Faraday ellipticity) of the transmitted light [13,14]. In principle, the Faraday effect originates from optical transitions and free carriers in a magnetic field [1]. For an isotropic sample in the Faraday geometry, Faraday rotation results from differing indices of refraction for left- and right-circularly polarized light, where a difference in absorption for left- and right-circularly polarized light produces Faraday ellipticity. In non-isotropic cases, Faraday ellipticity can also arise from stress-induced linear birefringence [15], or linear magnetic birefringence [16].

The MIR energies used in this experiment are up to an order of magnitude smaller than the band gap energy of the semiconductors and insulators studied here. In general, there will be no absorption of light in this energy range. When a magnetic field is applied to a sample the interband transition energies will shift, causing a difference in the indices of refraction for left- and right-circularly polarized light below the band gap. A phase shift in left- and right-circularly polarized waves is induced by this difference, which causes a polarization rotation in the transmitted light. This angle of rotation $\text{Re}(\theta_F)$ is proportional to the sample's thickness d and applied magnetic field H . The Faraday angle normalized by the field and sample

thickness is known as the Verdet coefficient ($V = \text{Re}(\theta_F)/(Hd)$). The Verdet coefficient for radiation below the band gap of an insulating sample has only interband contributions, and is proportional to λ^{-2} [17]. As mentioned earlier, Faraday ellipticity is not expected in these materials in the MIR regime, because the radiation energy is below the absorption edge. However, reproducible ellipticity signals proportional to H are found throughout our experiment, which scales the same as the polarization rotation [see Eqs. (2) and (6)]. Note that Faraday ellipticity is defined as the ratio of the minor to major axes of the polarization ellipse. In this study, we suggest that the observed ellipticity arises from the rotation of the polarization incident on optical components after the sample (e.g., photoelastic modulator (PEM), windows, substrates, lenses, etc...). It is important to better understand this ellipticity artifact so that we may isolate the real signal produced by the sample. For example, one similar artifact that we previously found was that stray magnetic fields can induce rotation and ellipticity signals in the output of gas lasers that are comparable to the signals produced by samples [14]. This artifact is easily removed by placing the lasers farther away from the magneto-optical cryostat [14].

In this paper, we present the MIR complex Faraday angle measurements of GaAs, BaF₂, LaSrGaO₄, LaSrAlO₄, and ZnSe. We shall first introduce the magneto-optical measurement setup, focusing on our newly custom-modified prism monochromator. Next, we determine the Verdet coefficients of these samples and analytically derive the static retardance of optical components from the rotation and ellipticity signals. Finally, we discuss new calibration techniques and some important artifacts, including the static retardance of our PEMs and other optical components, such as windows and polarizers.

2. EXPERIMENTAL TECHNIQUE

There are two ways in which linearly polarized light can change after interacting with a sample in a magnetic field. The plane of the polarization can rotate, and the light can acquire ellipticity. These polarization changes in the transmitted light are characterized by the complex Faraday angle θ_F .

Our gas lasers (CO₂, 9–11 μm ; CO, 5–6 μm ; HeNe, 3.4 μm) are set up as described in [14]. However, for this work we have expanded the number of usable laser lines with new semiconductor lasers (wavelengths 2.5, 2.0, 1.5, 1.3, and 0.978 μm). These lasers provide Faraday angle measurements throughout a wide range of discrete energies (0.1 eV – 1 eV). To further expand the capabilities of our system we have also added a new custom-modified double-pass prism monochromator (Perkin-Elmer Model 99) with a 300 W Xe lamp (Perkin-Elmer Cermax), which allows continuous broadband measurements in the 0.28 – 1.5 eV energy range. Unlike typical arc lamps, which are housed in glass and therefore cannot be used beyond 2 μm , our Cermax arc lamp housing contains a sapphire window, which is transparent out to 6 μm . Furthermore, standard globar sources tend to have large radiating areas compared to the output power and color temperatures near 1000 K (e.g., the 140 W Newport/Oriel model 6363 infrared emitter has a color temperature below 1100 K and a radiating area of 6.4 mm \times 17.5 mm). Our arc lamp has a significantly smaller source area (arc gap is approximately 1 mm and the radiating area is even smaller) and a color temperature of 6000 K. This smaller source size translates into a much brighter il-

lumination spot on the sample (5 mm \times 5 mm) compared to typical globar sources, which tend to overfill the sample when imaged onto it. Based on Planck's black body radiation law, the sixfold increase in color temperature alone increases the intensity of light from the Cermax arc lamp at wavelengths of 2 μm and 4 μm by factors of 600 and 40, respectively. The critical advantage of the double-pass prism monochromator is that it relies on a CaF₂ prism to disperse the radiation instead of a diffraction grating, which is used in most new monochromators. The prism refracts each wavelength into a unique angle, which is not the case with diffraction gratings. For example, with a grating the first-order diffraction peak position for a wavelength of 2 μm will also contain the second-order peak for 1 μm wavelength light. When scanning wavelengths from 1 to 5 μm using a grating, one would need to use a series of short-wavelength cut-off filters to remove the higher-order peaks from shorter wavelengths (which typically are more intense, since the source output intensity drops at longer wavelengths). This is not only cumbersome and expensive, but it also reduces the throughput of the system. It should be noted that, for our setup, we are reversing the beam path through the monochromator in order to use it as a source instead of an analyzer, i.e., light exits the original entrance slit (Slit 2 in Fig. 1).

Figure 1 shows the optical path of our broadband light source (a detailed description of the gas laser beam path is found in Ref. [14]). First, light from the Xe arc lamp is focused onto Slit 1. The light is then collimated by a parabolic mirror and sent to the CaF₂ prism. The light passes through the prism four times before exiting the monochromator at Slit 2. The desired probe wavelength is chosen by rotating the prism. The wavelength of light that exits Slit 2 has been calibrated in the 4.4 μm – 0.95 μm range with a Bomem Fourier transform infrared spectrometer using an InSb detector. A grating monochromator and photomultiplier tube detector were used to calibrate wavelengths from 0.95 μm – 0.63 μm (the grating monochromator was calibrated using Hg and Kr lamps). The spectral profile of the broadband source's output beam is shown in the inset of Fig. 1. Note that the side lobes of the profile are reminiscent of an Airy function used to describe a single slit diffraction pattern in real space and are consistent with the convolution of the spatial and spectral profiles of the source aperture. The spectral linewidth in the 4.4 μm – 0.95 μm range is 50 nm or less using 0.05 inch slit widths. For the 0.95 μm – 0.63 μm region the linewidth is about 20 nm with 0.02 inch slit widths. After emerging from the monochromator, the light is vertically polarized (i.e., oriented along the x axis) by polarizer P₁ as shown in Fig. 1.

The sample is located in a magneto-optical cryostat, which can reach temperatures down to 6 K and magnetic fields up to 7 T. When using gas lasers, the cryostat is fitted with two ZnSe windows mounted on 30 cm extension tubes. This large distance from the cryostat reduces Faraday rotation produced in the windows by stray magnetic fields interacting with the windows. The sample substrate and the ZnSe windows are wedged 1° – 2° to prevent étalon artifacts from multiple reflections. For the broadband setup unwedged 2.5 inch BaF₂ windows are attached directly to the cryostat tail piece without any extension tubes. Unlike with coherent laser radiation, we expect artifacts due to multiple reflections of incoherent broadband light in the BaF₂ windows to be small. The stray

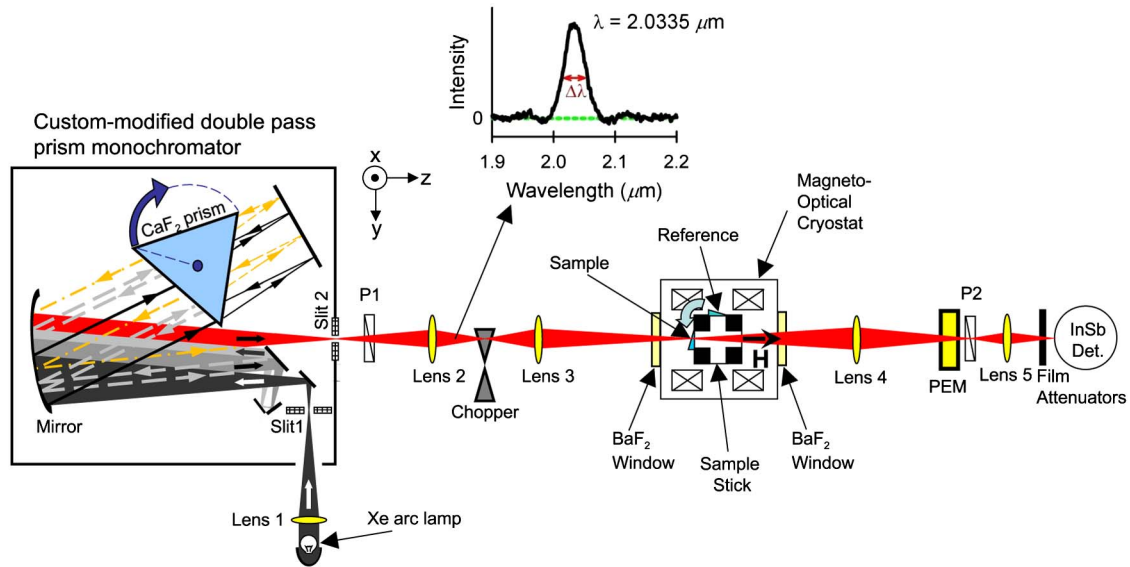


Fig. 1. (Color online) Overall schematic of the optical path, as viewed from above. The beam passes the CaF_2 prism four times: thick line with arrow (beam before prism), thin line with arrow (first pass), thick dashed line with arrow (second pass), thin dashed line with arrow (third pass), and dot-dashed line with arrow (fourth pass). The wavelength exiting the monochromator is selected by rotating the prism. The spectral profile of the exit beam is shown for $2\ \mu\text{m}$ wavelength radiation in the inset. $\Delta\lambda$ represents the spectral linewidth. The sample stick can be rotated to select sample or reference material.

magnetic field is estimated to be approximately 0.01 T at the ZnSe windows and 0.3 T at the BaF_2 windows when the field at the center of the magnet is 1 T. We are now using extension tubes for the BaF_2 windows to reduce the background rotation produced by these windows.

The PEM modulates the relative phase of the two orthogonal linear polarization components that pass through it. It is this modulation that allows us to determine the polarization of the beam that passes through the sample. The types of PEMs and polarizers used in the system depend on the probe wavelength. In the $4.44 - 2\ \mu\text{m}$ wavelength range, we used a ZnSe PEM (II/ZS50, Hinds Instruments) in combination with two BaF_2 holographic wire-grid polarizers (Thorlabs WP2SH-B) labeled as P_1 and P_2 , respectively, in Fig. 1. For the $2 - 0.63\ \mu\text{m}$ wavelength range, we used a fused silica PEM (I/FS50, Hinds Instruments) and calcite Glan-Taylor polarizers (MGTYA 20, Karl Lambrecht Corporation). To keep multiple reflections within the PEM from reaching the detector the ZnSe PEM is tilted forward 25° and the fused silica PEM crystal is wedged. The optical axis of the PEM is oriented along the x axis, which is the same orientation as the incident light polarization shown in Figs. 1 and 2. After passing through the sample, the transmitted light acquires a small y -component of polarization, which produces rotation and ellipticity. The PEM modulates the phase of this y component of polarization with respect to the x component at a frequency $\omega_{\text{PEM}} \approx 50 \times (2\pi)$ kHz. The PEM modulates the phase difference between the x and y components of the transmitted light sinusoidally: $\delta(t) = R_d \cos(\omega_{\text{PEM}}t)$, where R_d is the dynamic retardance amplitude. A linear polarizer (P_2) placed after the PEM is oriented at $\alpha_2 = 45^\circ$ with respect to the x axis to mix the x and y polarization components of the light exiting the PEM.

The intensity of the modulated light is measured by a liquid-nitrogen-cooled detector. Mercury-cadmium-telluride (MCT) and InSb detectors are used for the lasers and the broadband light source, respectively. Three lock-in amplifiers are used to obtain the complex Faraday angle. One lock-in amplifier is

referenced to the chopper frequency ω_0 (~ 1 kHz) in order to measure the overall light intensity. The two others are locked onto the even and odd harmonics of ω_{PEM} in order to detect the polarization of the beam. The even harmonics of ω_{PEM} are related to the rotation $\text{Re}(\theta_F)$ while the odd harmonics are related to the ellipticity $\text{Im}(\theta_F)$ [13]:

$$\text{Re}(\theta_F) = \frac{I_{2\omega_{\text{PEM}}}}{4J_2(R_d)I_0}, \quad \text{Im}(\theta_F) = \frac{I_{3\omega_{\text{PEM}}}}{4J_3(R_d)I_0}, \quad (1)$$

where J_n is the n th order Bessel function, $I_{n\omega_{\text{PEM}}}$ is the intensity of the light modulated at $n\omega_{\text{PEM}}$, and I_0 is the intensity of light modulated at the chopper frequency. Note that the Faraday rotation and ellipticity can also be measured using balanced detection schemes [18,19].

All samples are polished with a wedge in order to separate internal multiple reflections. The amount of wedging depends on the material. The wedge angle and thickness of our samples are as follows: for the 0.51 mm thick GaAs sample, a 1° wedge is used, while the BaF_2 , LaSrGaO_4 , and LaSrAlO_4 samples are wedged by 2° with average thicknesses of 0.81 mm, 0.38 mm, and 0.40 mm, respectively. Faraday measurements are also performed on the windows without a sample. Two ZnSe windows are wedged 2° , each with an average thickness 5 mm. All of these samples/windows show Faraday rotation as well as ellipticity in the MIR energy range.

The Verdet coefficient for below band gap radiation, which characterizes the polarization rotation produced by a material per unit thickness per unit magnetic field, has two terms. The first term is due to the interband absorption resonance and scales with the light wavelength as $1/\lambda^2$. The second term is due to free carrier interaction with radiation and scales as λ^2 . For below band gap radiation the Verdet coefficient can be expressed as [17]

$$V(\lambda) = \frac{\text{Re}[\theta_F(\lambda)]}{Hd} = \frac{u}{\lambda^2} + v\lambda^2, \quad (2)$$

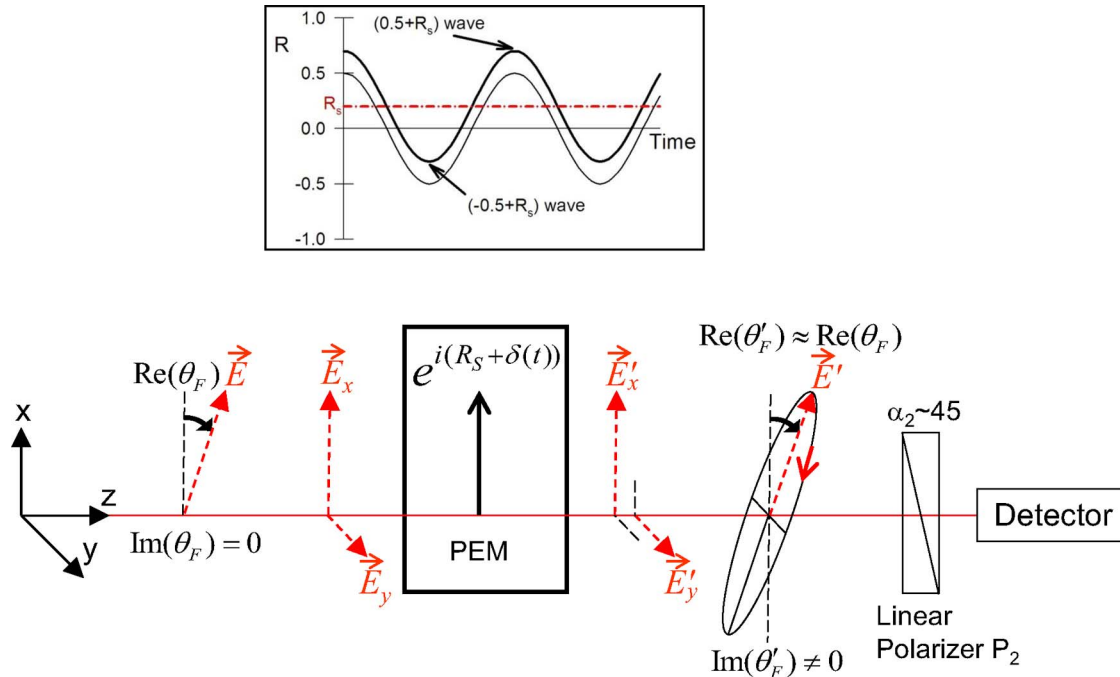


Fig. 2. (Color online) Optical path of the light after passing through the sample. Dashed arrows show the electric field vector. The time-dependent PEM dynamic retardance (thin line) is shown in the boxed inset when one sets the PEM retardance to 0.5 wave. Dot-dashed line in the inset represents the PEM's static retardance R_s . The total retardance (thick line) is shifted by R_s .

where u is the coefficient related to the interband contribution and ν is the free carrier contribution coefficient. The insulating samples probed in this experiment have extremely small free carrier densities, thus the interband transition term dominates, and one can expect the Verdet coefficients of the different semiconductors and insulators to have the same slope in a log-log plot of $V(\lambda)$. Interband Faraday rotation arises from the difference in index of refraction of right n_+ and left n_- circularly polarized light. The Faraday rotation angle per unit path length is $\theta_F = (\omega/2c)(n_- - n_+)$ where ω is the probing radiation frequency and c is the speed of light. For a small energy Zeeman splitting ΔE of the left and right circularly polarized interband optical transitions produced by a magnetic field, the difference $(n_- - n_+)$ is small and linearly increasing with energy far below the gap energy (E_g) so that $(n_- - n_+) = (\partial n/\partial E)\Delta E$ where n is the index of refraction without magnetic field, and we have assumed that the oscillator strengths of the transitions have not changed. The first term $(\partial n/\partial E)$ is proportional to E/E_g far below the band edge and to higher orders of E/E_g near the band edge. The energy difference ΔE between the circularly polarized interband transitions is associated with the magnetic-field-induced Zeeman splitting of the chiral states at the band edge. Therefore, ΔE is proportional to $\mu B \propto B/m_{\text{band}}$ where μ is the magnetic moment and m_{band} is the band mass of the electron/hole. Since ΔE does not depend on the probing energy, this derivation is consistent with Eq. (2), and the Faraday angle can be expressed as

$$\theta_F \propto \frac{E^2}{m_{\text{band}}} \propto \frac{1}{m_{\text{band}}\lambda^2}. \quad (3)$$

Equation (3) shows that the Faraday rotation increases as the band mass decreases, due to the larger magnetic dipole moment, and hence larger Zeeman splitting for smaller band masses.

For below band gap radiation, the MIR Faraday ellipticity of these materials will be negligibly small ($\text{Im}(\theta_F) \approx 0$) because there is no absorption. However, Faraday ellipticity is commonly observed due to other components in the system (e.g., as previously mentioned stray magnetic fields interacting with a gas laser can produce Faraday ellipticity [14]). Ellipticity can also be produced by the PEM's static stress-induced birefringence. In this case, the PEM acts like a static wave plate with a static retardance R_s caused by non-homogeneous mounting stresses on the PEM crystal. This static retardance causes a shift in the dynamic retardance R_d by a constant as shown by the inset in Fig. 2. Note that the optical axis of the static retardance may be oriented differently than the dynamic retardance axis, but in this paper we simply consider the case where the two optical axes have the same orientation. The net retardance of the PEM is given by

$$R_{\text{PEM}}(t) = \delta(t) + R_s. \quad (4)$$

We assume that the light transmitted by the sample experiences Faraday rotation only (i.e., $\text{Im}(\theta_F) = 0$). After passing through the sample, the PEM, and P_1 , the light containing signals I_0 and $I_{\omega_{\text{PEM}}}$ is incident on the detector. The lock-in amplifiers then pick off the intensity of the two PEM harmonics with frequencies $2\omega_{\text{PEM}}$ and $3\omega_{\text{PEM}}$. The intensity ratio of the two signals produces

$$\frac{I_{3\omega_{\text{PEM}}}}{I_{2\omega_{\text{PEM}}}} = \frac{J_3(R_d)}{J_2(R_d)} \tan(R_s). \quad (5)$$

Equation (5) is equivalent to the static retardance formula obtained from the intensity ratio of $I_{\omega_{\text{PEM}}}$ and $I_{2\omega_{\text{PEM}}}$ in [15]. The ratio $\text{Im}(\theta_F)/\text{Re}(\theta_F) = (I_{3\omega_{\text{PEM}}}J_2(R_d))/(I_{2\omega_{\text{PEM}}}J_3(R_d))$ shown in [13] allows Eq. (5) to be simplified as

$$\text{Im}(\theta_F) = \text{Re}(\theta_F) \tan(R_s). \quad (6)$$

Equation (6) shows that the real part of the Faraday angle is connected to the imaginary part by the PEM's static retardance. This implies that any optical element with a static retardance, such as a PEM, placed after the sample can convert a pure rotation in polarization into ellipticity. Furthermore, the static retardance can be expressed as $\Delta L/\lambda$, where ΔL is the optical path difference produced by R_s , e.g., mounting stress. Although the effective ΔL can depend on wavelength [20], we assume that it is constant here to obtain the first-order behavior of $\text{Im}[\theta_F(\lambda)]$. For below band gap radiation in insulating samples, $\text{Im}(\theta_F)$ becomes

$$\text{Im}[\theta_F(\lambda)] = \frac{u}{\lambda^2} \tan(2\pi \frac{\Delta L}{\lambda}) \propto \frac{\Delta L}{\lambda^3}, \quad (7)$$

where we have assumed that $\Delta L/\lambda \ll 1$. Therefore, one sees that the Faraday ellipticity artifact originates from Faraday rotation, and that this ellipticity will roughly scale as $1/\lambda^3$.

3. VERDET COEFFICIENTS

We measure Verdet coefficients for materials that are commonly used as substrates and windows over a wide energy range from MIR to visible (0.1 – 1.5 eV). Ellipticity artifacts caused by the static retardance of the PEM and other optical components are also described. The samples do not induce ellipticity in the MIR. However, our measurements and analysis confirm that the PEM's static retardance can translate rotations into ellipticity signals.

Figure 3 shows θ_F for GaAs, BaF₂, LaSrGaO₄, LaSrAlO₄, and ZnSe normalized by the magnetic field H as a function of wavelength λ in a log–log plot. These Faraday angles are measured using both laser and the broadband sources for GaAs, BaF₂, and LaSrAlO₄, whereas only lasers are used for the other samples. θ_F produced by these samples increases as the wavelength shortens. For $\text{Re}(\theta_F)$, there is a difference of approximately two orders of magnitude between longer and shorter wavelengths: 10^{-4} to 10^{-2} rad for GaAs, and 10^{-5} to 10^{-3} rad for the other materials. The $\text{Im}(\theta_F)$ varies by three orders of magnitude for GaAs ranging from 10^{-5} to 10^{-2} rad. The noise floor for both $\text{Re}(\theta_F)$ and $\text{Im}(\theta_F)$ is approximately 10^{-5} rad, so the decay of these signals at longer wavelengths is lost in the noise for the BaF₂, LaSrGaO₄, ZnSe and LaSrAlO₄ samples. For comparison, typical Faraday signals for non-ferromagnetic metals are on the order of 10^{-4} rad at 8 T and 100 meV [6,21]. For ferromagnetic metals such as the ruthenate perovskite SrRuO₃ and the diluted magnetic semiconductor Ga_{1-x}Mn_xAs films, the Faraday angles are on the order of 10^{-2} rad at 1 T from 0.1 – 0.8 eV [14]. At longer wavelengths ($\sim 10 \mu\text{m}$), Faraday angles from ferromagnetic metallic films ($\sim 100 \text{ nm}$ thick) usually dominate the signal, but the $\text{Re}(\theta_F)$ from the substrates and windows becomes more important as the wavelength is decreased. The vertical dashed line at $\lambda = 2 \mu\text{m}$ in Fig. 3 marks the boundary of the two different PEM/polarizer sets. Interestingly, the $\text{Re}(\theta_F)$ is continuous across the boundary, while the $\text{Im}(\theta_F)$ shows a clear discontinuity at the boundary. However, the slope for $\text{Im}(\theta_F)$ is similar on both sides of the boundary. This implies that the ellipticity does not come from the sample itself, but rather it is

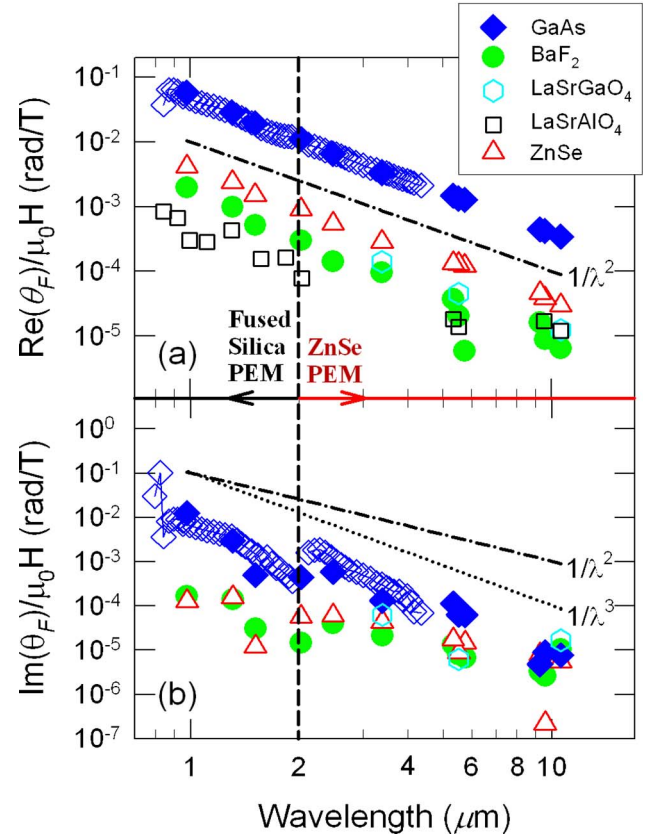


Fig. 3. (Color online) The log–log plot of the (a) $\text{Re}(\theta_F)$ and (b) $\text{Im}(\theta_F)$ divided by the magnetic field H as a function of wavelength λ . The vertical dashed line divides the regions where the two different PEM/polarizers are used. For GaAs, the solid diamonds represent laser measurements and open diamonds represent broadband measurements. Dot-dashed line and dotted line are guides to the eye indicating $1/\lambda^2$ and $1/\lambda^3$ dependence, respectively.

an artifact caused by the PEM, polarizers, and/or windows, which are different in the two measurement ranges.

The wavelength dependence of $\text{Re}(\theta_F)/H$ is shown in Fig. 3(a). According to Eq. (2) the slope of these data determine to which power λ is raised in Eq. (2), which is expected to be -2 for below band gap radiation in insulating materials. Table 1 shows the gap energies of the samples, which are larger than the probe energies used in this experiment (0.1 – 1.5 eV). The only exception is for GaAs, which has an energy gap of 1.43 eV. This results in the data deviating from Eq. (2) near the band gap energy of GaAs in Figs. 3 and 4. The dot-dashed reference line in Fig. 3 acts as a guide indicating a $1/\lambda^2$ dependence. All samples produce a slope near -2 as shown in Table 1, but the slope of the BaF₂ data deviates more than the others, probably due to the noise from the weak Faraday signals (10^{-5} rad, at 1 T) at wavelengths longer than $5 \mu\text{m}$. Faraday measurements using the broadband light source in GaAs (open diamonds) cover the regions between laser points (solid diamonds), which demonstrates that the measurements using various light sources are in good agreement with one another.

To further clarify the wavelength dependence of the Verdet coefficient, one can plot $V(\lambda)$ as a function of $1/\lambda^2$. Figure 4 shows $V(\lambda) = \text{Re}(\theta_F)/(Hd)$ from GaAs as a function of $1/\lambda^2$. As expected the data show a linear dependence for below gap

Table 1. Verdet Coefficients ($V(\lambda) \propto \lambda^\alpha$, $V(\lambda) = u/\lambda^2$)

Material	E_{gap} (eV)	α (Theory $\alpha = -2$)	u ($^\circ\mu\text{m}^2/\text{Tm}$)	$u_{10.5\mu\text{m}}$ ($^\circ/\text{Tm}$)	Ref. $u_{10.5\mu\text{m}}$ ($^\circ/\text{Tm}$)
GaAs	1.43 ^a	-2.108	5725 \pm 1050	51.93 \pm 9.56	44 ^b
BaF ₂	11.0 ^c	-2.523	111 \pm 46	1.00 \pm 0.42	
LaSrGaO ₄	2.85 – 2.87 ^d	-2.086	195 \pm 15	1.77 \pm 0.13	1.5 ^b
LaSrAlO ₄	2.84 – 3.0 ^d	-1.873	72 \pm 38	0.65 \pm 0.34	
ZnSe	2.7 ^e	-2.010	2242 \pm 165	20.3 \pm 6.1	24.4 ^f

^aRef. [22].^bRef. [13].^cRef. [23].^dRef. [24].^eRef. [25].^fRef. [26].

radiation and become non-linear when the gap energy is approached.

The constant u in Eq. (2) is related to the energy gap and can be determined by the slope in Fig. 4. The measured values of Verdet coefficient are shown in Table 1. The units of u are ($^\circ\mu\text{m}^2$)/(Tm); however, one usually considers the Verdet coefficient at a specific wavelength, so the constant u often has units $^\circ/\text{Tm}$ at a particular wavelength. Typically, lower gap energies produce larger values of u . For example, GaAs, with an energy gap half as large as that of ZnSe, has double the Verdet constant. Likewise, BaF₂, which has an energy gap that is an order of magnitude larger than the gaps in ZnSe and GaAs, has a Verdet coefficient that is an order of magnitude smaller. However, LaSrGaO₄, LaSrAlO₄, and ZnSe have almost identical gap energies, but u for ZnSe is an order of magnitude larger. According to Eq. (3), the interband Faraday rotation is proportional to $1/m_{\text{band}}$ when the probing radiation energy is much smaller than the band gap. Comparing measurements of $n(E)$ for ZnSe, LaSrGaO₄ and LaSrAlO₄, we find that they all have similar values for $\partial n/\partial E$ in our measurement range. However, the conduction band mass of ZnSe is approximately an order of magnitude smaller than that of LaSrGaO₄ and LaSrAlO₄, and therefore we expect that the magnetic dipole moment, and hence the Zeeman splitting ΔE and θ_F (or u) are significantly larger for ZnSe than for LaSrGaO₄ and LaSrAlO₄.

Our measurements of u are in good agreement with other published data at 10.5 μm as can be seen in Table 1. The ZnSe

measurements were only made with windows rather than samples made of this material. The windows are located a significant distance away from the center of the magnet (~ 60 cm), therefore the magnetic field had to be estimated using the stray field plots for our magnet. This leaves us with a fairly large uncertainty ($\pm 30\%$) in the Verdet values for ZnSe. To the authors' best knowledge, this work is the first reported measurement of the MIR Verdet coefficients for BaF₂ and LaSrAlO₄. Note that 12 $^\circ/\text{Tm}$ reported for LaSrGaO₄ in [13] is a typographical error, which should read 12 $^\circ/\text{m}$ at 8 T.

Figure 3(b) shows $\text{Im}(\theta_F)$, which like $\text{Re}(\theta_F)$ scales as a power of λ . In Eq. (7), $\text{Im}(\theta_F)$ has a $1/\lambda^3$ dependence when the PEM acts like a static waveplate, thereby producing an ellipticity. When compared to the reference lines in the plot, it is quite clear that the GaAs data has a $1/\lambda^3$ dependence (except near 2 μm as will be discussed later). There is also a clear discontinuity in these data, which results from the different PEMs having different static retardances. The slopes, however, are similar in the two regions. Unfortunately, ellipticity from the other samples is noisy due to weak Faraday signal near 10^{-5} rad, but the data are consistent with $1/\lambda^3$ below 2 μm where the magnitude of the signal is well above 10^{-5} rad. The ellipticity artifact is approximately two orders of magnitude smaller than the rotation signal but can be important in materials which produce large Faraday rotation and small Faraday ellipticity.

4. DISCUSSION

In this section, we introduce a retardance calibration technique, which provides a more reliable polarimetry system calibration. We also discuss the sensitivity of Faraday measurements using our system and explore ellipticity artifacts.

A. Calibration

We previously developed a calibration technique to simultaneously determine both R_d and the orientation angle α_2 of the final linear polarizer P_2 [14]. The calibration and all measurements are performed near $R_d = 2.406$ rad with $\alpha_2 = 45^\circ$. The calibration is performed by rotating the PEM and P_2 by a known angle as a single unit. The changes in the $2\omega_{\text{PEM}}$ and $4\omega_{\text{PEM}}$ signals allow us to determine R_d and α_2 .

In this study we find that this calibration technique produces errors (as indicated by variations in α_2 , which should remain constant) when the extinction ratio of the linear polarizers in the system is less than 100:1. Therefore, we developed an independent test to determine R_d . We mount a static waveplate with retardance R_w on a rotating stage in front of the

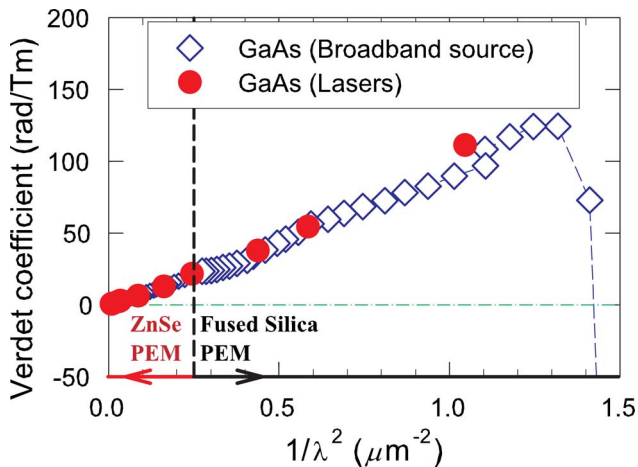


Fig. 4. (Color online) Verdet coefficient of GaAs as a function of $1/\lambda^2$. Note that the wavelength dependence deviates for $1/\lambda^2$ near the band edge at 1.4 eV.

PEM. The stage is then rotated with frequency $\omega_0 \approx 27 \times (2\pi)$ Hz, which is much lower than the PEM modulation frequency $\omega_{\text{PEM}} = 50 \times (2\pi)$ kHz. Equations (14a) and (14b) in [13] reveal that the intensity $I_{4\omega_0}$ at the 4th harmonic of ω_0 can be expressed as a function of R_d ,

$$I_{4\omega_0}(R_d) = \frac{1}{2} J_0(R_d) (1 - \cos(R_w)), \quad (8)$$

where J_0 is the zeroth-order Bessel function. One can adjust R_d of the PEM while spinning the wave plate to find the PEM retardance where $I_{4\omega_0}(R_d) = 0$, which is also where $J_0(R_d) = 0$. Since $I_{4\omega_0}(R_d) = 0$ when $J_0(R_d) = 0$, regardless of the value of R_w , the key advantage of this technique is that its accuracy does not depend on how well R_w is known. The only requirement is that the $R_w \neq 0$. In our case, we used a waveplate with $R_w = 0.25$ wave at $0.8 \mu\text{m}$.

These two calibration techniques provide a more reliable determination of R_d for our polarimetry system. When using light with a wavelength of $1.3 \mu\text{m}$ or shorter we find that the actual retardance of the fused silica PEM is accurate to within 5% when set to 2.406 rad. It was found that, when using wavelengths longer than $1.3 \mu\text{m}$, the PEM reaches a physical upper limit before getting to the desired 2.406 rad. The maximum optical path difference for the fused silica PEM is $\Delta L_{\text{max}} = 0.49 \mu\text{m}$. The retardance which saturates the PEM can be determined by $R_d^{\text{max}}(\lambda) = (2\pi\Delta L_{\text{max}})/\lambda$. Any set retardance that is greater than R_d^{max} will default to this maximum value.

Conversely, the ZnSe PEM cannot drive any retardance lower than R_d^{min} (i.e., the retardance hits a floor and the PEM crystal cannot be driven at smaller amplitudes). The minimum optical path difference for the ZnSe PEM is $\Delta L_{\text{min}} = 0.401 \mu\text{m}$. This corresponds to a critical wavelength of $1.047 \mu\text{m}$ where the retardance of 2.406 rad is still attainable. The ZnSe PEM had a retardance accuracy that is comparable to the fused silica. For wavelengths greater than $1.047 \mu\text{m}$, the set 2.406 rad retardance is accurate to within 5%. The ZnSe PEM also has an upper limit to the retardance, however, in this paper we are not using wavelengths where this upper limit would be reached.

Since the angle between the PEM and P_2 is kept constant throughout all measurements, the calibrated angle α_2 should remain constant at 45° for all laser wavelengths. For the broadband light source, one has even stronger expectations that the calibrated α_2 must be the same for all wavelengths because the optical alignment does not change while varying the wavelength, which is not strictly true when different lasers are used. Below $2 \mu\text{m}$ with the fused silica PEM, the calibrated angle α_2 is $45^\circ \pm 3\%$ for all wavelengths. For the ZnSe PEM, α_2 is found to be $45^\circ \pm 5\%$ for all wavelengths except between $1.36 \mu\text{m}$ to $2.21 \mu\text{m}$. In order to maintain a high extinction ratio, wire-grid polarizers (at the spectrometer exit slit and after the PEM) are used for wavelengths greater than $1.78 \mu\text{m}$ and calcite Glan-Taylor polarizers are used below $2 \mu\text{m}$. Part of the problem in using the ZnSe PEM below $2 \mu\text{m}$ is that its anti-reflection coating, which is designed for $9 - 11 \mu\text{m}$ wavelength radiation, strongly absorbs radiation around $2 \mu\text{m}$. The poor calibration accuracy in certain wavelength ranges is strongly correlated to poor polarizer extinction ratios and low light intensity such as near $2 \mu\text{m}$ with the ZnSe PEM. We have also seen irregular behavior in α_2 with the calcite polarizers as the extinction ratio decreases. The extinction ra-

tio for the calcite polarizer drops below 60:1 in the $1.36 \mu\text{m}$ to $2.21 \mu\text{m}$ wavelength range. In this wavelength range, α_2 obtained from calibration measurements linearly increases from 45° to 55° as the extinction ratio decreases, despite the fact that P_2 is held at a fixed angle. Near $3 \mu\text{m}$, where the calcite polarizer has a good extinction ratio again, α_2 is found to be at its nominal value of 45° .

It is important to also realize that calcite polarizers have a limited acceptance angle for which incident light is properly polarized. This acceptance angle is asymmetric and depends on the wavelength. At shorter wavelengths around $0.66 \mu\text{m}$, our calcite polarizers have symmetric acceptance angles of approximately 4° away from normal incidence. However, at longer wavelengths, the acceptance angles are asymmetric. For $2 \mu\text{m}$, one of the acceptance angles is 2° and the other is 6° from normal. The wavelength-dependent acceptance angles could allow parts of the beam that were inside the acceptance cone at one wavelength to be outside the acceptance cone at a different wavelength thereby creating a poor extinction ratio and a poor calibration.

B. Sensitivity of the Polarimetry System

Figure 3 shows that data scatters below 10^{-5} rad due to noise. For lasers, the noise is less than 5×10^{-5} rad for all wavelengths. Since the broadband light source is much less intense than the lasers, the sensitivity is closer to 10^{-4} rad.

C. Artifacts

As mentioned earlier the most striking artifact that we discovered is the ellipticity signal that arises from real polarization rotation. This artifact is manifested in a $\text{Im}(\theta_F)$ that is proportional to $1/\lambda^3$ and is caused by optical elements in the system behaving like a static waveplate with retardance R_s . Equation (6) shows the connection between the real and imaginary parts of the Faraday angle through R_s . We have determined this static retardance R_s experimentally by taking the ratio of $\text{Im}(\theta_F)$ and $\text{Re}(\theta_F)$ when the PEM or the laser polarization axis is rotated. Figure 5 shows the static retardance R_s as a function of wavelength. In GaAs, the values of R_s determined by the laser and broadband light sources agree with each other. In Eq. (7), we see that R_s follows a $1/\lambda$ dependence. However, the best fit for our data (represented by the dashed line in Fig. 5) reveals a $1/\lambda^{1.45}$ behavior for the ZnSe PEM. It is possible that our measured value of the exponent differs from the expected value of 1 because ΔL also has a wavelength dependence. The static retardances of the two different PEMs are different from each other, since they are composed of different materials that are mounted in different housings. In order to ensure that the Faraday ellipticity is not produced by the sample, one can perform the same tests by making pure mechanical rotations of the PEM and P_2 by a small angle φ as one unit without a sample and no magnetic field. This is equivalent to the laser polarization axis rotating the same amount in the opposite direction ($-\varphi$). In Fig. 5, the open triangles represent the static retardance deduced by this pure mechanical rotation of the PEM and P_2 . The static retardances of the ZnSe and fused silica PEMs that are determined by pure rotations are consistent with the ellipticity induced by Faraday rotation from the sample in a magnetic field. We suspect that the anomalous behavior of the measured static retardance for the ZnSe PEM below $2.21 \mu\text{m}$ is related to the

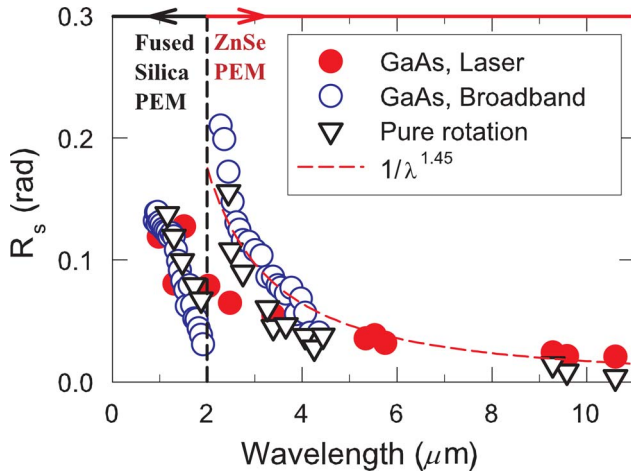


Fig. 5. (Color online) Static retardance R_s determined from Faraday rotation produced by the GaAs sample in a magnetic field (circles) and from the mechanical rotation of the PEM/polarization without a magnetic field (triangles) as a function of wavelength. The red dashed curve is a fit performed above $2 \mu\text{m}$.

strong absorption of radiation by its anti-reflection coating in this range.

The static retardance of the PEM can be measured directly by placing the PEM between two crossed polarizers. The PEM optical axis is oriented at 45° with respect to the polarizers. With the PEM turned off, any small static retardance in the PEM allows higher transmission through the crossed polarizers. Typically, the static retardance of a waveplate oriented at 45° between two crossed polarizers can be obtained by the simple formula, $I = (I_0/2)(1 - \cos(R_s))$, where I is the intensity of incident light, I_0 is the maximum intensity when the two polarizers are parallel, and R_s is the static retardance. Static retardances, $R_s = 0.055$ rad at $5.5 \mu\text{m}$ and $R_s = 0.022$ rad at $10.6 \mu\text{m}$, are measured for our ZnSe PEM using the crossed polarizer method. The uncertainty in these measurements is fairly large, since R_s depends on which part of the PEM is illuminated and how the PEM is tilted. These values are comparable to those reported in Fig. 5, where R_s is 0.038 rad at $5.5 \mu\text{m}$, and the average R_s is 0.01 rad at $10.6 \mu\text{m}$. The second method is to measure the constant offset in the overall PEM dynamic retardance by using a tunable waveplate while the PEM is energized. By tilting the tunable waveplate (tunable zero-order phase retardation plates, Alphalas) we can vary the ellipticity of the transmitted light. We calibrated R_s^{WP} of the tunable waveplate independently by placing it between crossed polarizers, as described in the first calibration method. The tunable waveplate and the PEM are both oriented at 45° between the two crossed polarizers. Asymmetry of the PEM driving retardance as shown in Fig. 2 is reflected in the $1\omega_{PEM}$ signal, which is proportional to the asymmetry in the PEM's polarization modulation. By tilting the tunable waveplate, one can adjust R_s^{WP} until it cancels R_s and thereby zero the $1\omega_{PEM}$ signal. We measure the tilt angle of the tunable waveplate to determine R_s^{WP} . At $5.53 \mu\text{m}$, the PEM retardance offset is 0.025 rad, which again is comparable to PEM R_s of 0.038 rad in Fig. 5.

5. CONCLUSION

We have presented complex Faraday angle measurements in GaAs, BaF₂, LaSrGaO₄, LaSrAlO₄, and ZnSe in the MIR energy

range well below the interband absorption edge. The wavelength dependence of the Faraday rotation agrees well with theory for a Verdet coefficient that is dominated by interband transitions. The constant u for the interband contribution in each sample is consistent with the values reported by others at $10.5 \mu\text{m}$. We suggest that the Faraday ellipticity in this experiment is an artifact resulting from Faraday rotation and anisotropic strain in the optical components after the sample. These components act as weak static waveplates, causing ellipticity changes when the sample produces Faraday rotation. The Faraday ellipticity seen in GaAs follows a $1/\lambda^3$ dependence, which is predicted by a simple calculation. The static retardance is obtained from the normalized signal ratio between the Faraday rotation and ellipticity. Furthermore, mechanical polarization rotations produce ellipticity signals comparable to those produced by rotations due to an applied magnetic field. These results are critical for removing the background contributions from GaAs, BaF₂, LaSrGaO₄, LaSrAlO₄, and ZnSe substrates and windows in MIR Faraday measurements. They also confirm the high accuracy of these measurements over the entire MIR wavelength range and indicate that pure rotation signals can produce false ellipticity signals.

ACKNOWLEDGMENTS

We thank H. D. Drew and R. L. Greene for providing us with LaSrGaO₄ and LaSrAlO₄ samples, B.D. McCombe and A.V. Stier for their assistance in performing the wavelength calibration of the broadband light source using their Fourier transform spectrometer, A. Petrou for supplying Hg and Kr lamps for wavelength calibration, and B. Wang from Hinds Instruments for helpful discussions about PEMs. We also thank A. G. Markelz for helpful discussions and A. Mukherjee for help in characterizing the PEM retardances. This work was supported by the Research Corporation for Science Advancement Cottrell Scholar Grant, National Science Foundation (NSF) NSF-CAREER-DMR0449899, and an instrumentation award from the College of Arts and Sciences, University at Buffalo.

REFERENCES

1. Yu.I. Ukhonov, "Magneto-optic Faraday effect in semiconductors," *Sov. Phys. Usp.* **16**, 236–250 (1973).
2. K. Ando, H. Saito, K.C. Agarwal, M. C. Debnath, and V. Zayets, "Origin of the anomalous magnetic circular dichroism spectral shape in ferromagnetic Ga_{1-x}Mn_xAs: impurity bands inside the band gap," *Phys. Rev. Lett.* **100**, 067204 (2008).
3. R. Chakarvorty, S. Shen, K.J. Yee, T. Wojtowicz, R. Jakiela, A. Barcz, X.Liu, J.K. Furdyna, and M. Dobrowolska, "Common origin of ferromagnetism and band edge Zeeman splitting in GaMnAs at low Mn concentrations," *Appl. Phys. Lett.* **91**, 171118 (2007).
4. G. Acbas, J. Cerne, J. Sinova, M. A. Scarpulla, O. D. Dubon, M. Cukr, and V. Novak, "A Comparison of the mid-infrared magneto-optical response of Ga_{1-x}Mn_xAs films grown by molecular beam epitaxy and ion implantation/laser melting," *J. Supercond. Nov. Magn.* **20**, 457–460 (2007).
5. G. Acbas, J. Cerne, M. Cukr, V. Novak, and J. Sinova, "Infrared magneto-optical studies in Ga_{1-x}Mn_xAs films," in *Physics of Semiconductors, Part B*, AIP Conference Proceedings 893 (), (AIP, 2007), p. 1217.
6. J. Cerne, M. Grayson, D. C. Schmadel, G. S. Jenkins, H. D. Drew, R. Hughes, A. Dabkowski, J. S. Preston, and P.-J. Kung, "Infrared Hall effect in high- T_c superconductors: evidence for non-Fermi-liquid Hall scattering," *Phys. Rev. Lett.* **84**, 3418–3421 (2000).

7. A. Zimmers, L. Shi, D. C. Schmadel, W. M. Fisher, R. L. Greene, H. D. Drew, M. Houseknecht, G. Acbas, M.-H. Kim, M.-H. Yang, J. Cerne, J. Lin, and A. Millis, "Infrared Hall effect in the electron-doped high-Tc cuprate $Pr_{2-x}Ce_xCuO_4$," *Phys. Rev. B* **76**, 064515 (2007).
8. K.S. Burch, D.D. Awschalom, and D.N. Basov, "Optical properties of III-Mn-V ferromagnetic semiconductors," *J. Magn. Magn. Mater.* **320**, 3207 – 3228 (2008).
9. G. Acbas, M.-H. Kim, M. Cukr, V. Novak, M.A. Scarpulla, O.D. Dubon, T. Jungwirth, J. Sinova, and J. Cerne, "Electronic structure of ferromagnetic semiconductor $Ga_{1-x}Mn_xAs$ probed by sub-gap magneto-optical spectroscopy," *Phys. Rev. Lett.* **103**, 137201 (2009).
10. J. Sinova, T. Jungwirth, J. Kucera, and A. H. MacDonald, "Infrared magneto-optical properties of (III,Mn)V ferromagnetic semiconductors," *Phys. Rev. B* **67**, 235203 (2003).
11. E. M. Hankiewicz, T. Jungwirth, T. Dietl, C. Timm, and J. Sinova, "Optical properties of metallic (III,Mn)V ferromagnetic semiconductors in the infrared to visible range," *Phys. Rev. B* **70**, 245211 (2004).
12. G. Acbas, J. Cerne, M. Cukr, V. Novak, and J. Sinova, "Infrared magneto-optical studies in $Ga_{1-x}Mn_xAs$ films," in *28th International Conference on the Physics of Semiconductors* (2006), pp. 1217 – 1218.
13. J. Cerne, D.C. Schmadel, L. B. Rigal, and H.D. Drew, "Measurement of the infrared magneto-optic properties of thin-film metals and high temperature superconductors," *Rev. Sci. Instrum.* **74**, 4755 – 4767 (2003).
14. M.-H. Kim, G. Acbas, M.-H. Yang, I. Ohkubo, H. Christen, D. Mandrus, M.A. Scarpulla, O.D. Dubon, Z. Schlesinger, P. Khalifah, and J. Cerne, "Determination of the infrared complex magneto-conductivity tensor in itinerant ferromagnets from Faraday and Kerr measurements," *Phys. Rev. B* **75**, 214416 (2007).
15. J.C. Cheng, L.A. Nafie, S.D. Allen, and A.I. Braunstein, "Photo-elastic modulator for the 0.55–13 μm range," *Appl. Opt.* **15**, 1960 – 1965 (1976).
16. K. Cho, S. P. Bush, D.L. Mazzoni, and C. C. Davis, "Linear magnetic birefringence measurements of Faraday materials," *Phys. Rev. B* **43**, 965 – 971 (1991).
17. G. Ruybbeck, W. Grevendonk, and P. Nagels, "Electron effective mass determination from intraband Faraday-rotation in silicon," *Physica B & C* **89**, 14 – 17 (1977).
18. G.B. Scott, D.E. Lacklison, H.I. Ralph, and J.L. Page, "Magnetic circular dichroism and Faraday rotation spectra of $Y_3Fe_5O_{12}$," *Phys. Rev. B* **12**, 2562 – 2571 (1975).
19. Y. Linzon, M. Ferrera, L. Razzari, A. Pignolet, and R. Morandotti, "Polarization proximity effect in isolator crystal pairs," *Opt. Lett.* **33**, 2871 – 2873 (2008).
20. J.P. Szczesniak, D. Cuddeback, and J.C. Corelli, "Stress-induced birefringence of solids transparent to 1- to 12- μm light," *J. Appl. Phys.* **47**, 5356 – 5359 (1976).
21. J. Cerne, D. C. Schmadel, M. Grayson, G.S. Jenkins, J.R. Simpson, and H. D. Drew, "Midinfrared Hall effect in thin-film metals: probing the Fermi surface anisotropy in Au and Cu," *Phys. Rev. B* **61**, 8133 – 8140 (2000).
22. C. Kittel, *Introduction to Solid State Physics*, 7th ed. (Wiley, (1996) p. 201.
23. G.W. Rubloff, "Far-ultraviolet reflectance spectra and the electronic structure of ionic crystals," *Phys. Rev. B* **5**, 662 – 684 (1972).
24. A. Jezierski, "Band structure of $LaSrGaO_4$ and $LaSrAlO_4$ compounds," *Phys. Stat. Sol. B* **207**, 183 – 189 (1998).
25. B. G. Streetman and S. K. Banerjee, *Solid State Electronic Devices*, 6th ed. (Pearson Prentice Hall, 2006), p. 540.
26. J. A. Wunderlich and L. G. DeShazer, "Visible optical isolator using ZnSe," *Appl. Opt.* **16**, 1584 – 1587 (1977).